Preliminary Assessment of a Distributed Electric Propulsion System for the SUSAN Electrofan

Leonardo Machado*, Timothy Chau†, and Gaetan K. Kenway‡
Science & Technology Corporation, M/S 258-2, Moffett Field, California, 94035

Jared C. Duensing§ and Cetin C. Kiris¶
NASA Ames Research Center, M/S 258-2, Moffett Field, California, 94035

The SUSAN Electrofan is a new hybrid electric large regional jet aircraft concept being studied by NASA that leverages advanced propulsion system technologies such as distributed electric propulsion (DEP) and boundary-layer ingestion (BLI) to reduce fuel consumption and emissions. In order to evaluate the individual benefits of these technologies toward the SUSAN Electrofan's wing-mounted propulsion systems, three configurations are proposed. The first consists of two underwing pylon-mounted podded propulsors and serves as a baseline, while the second features an underwing pylon-mounted DEP concept with 16 ducted fans in a mail-slot nacelle. The third and final configuration mounts the mail-slot nacelle directly onto the pressure side of the wing to also take advantage of BLI. This paper presents preliminary investigations into the design and performance of the first two propulsion system configurations. This begins with an initial propulsor and mail-slot design where the aeropropulsive design space is explored, and adverse effects are addressed through iterative geometry modifications. The propulsion system configurations are then installed onto a wing–body model to account for integration effects and assess the relative aerodynamic and shaft power performance of each concept. Results indicate the potential benefits of DEP, which come from significant reductions in total drag, provided by operation at much lower propulsor fan pressure ratios.

Nomenclature

α	=	Angle of attack
C_L	=	Lift coefficient
C_D	=	Drag coefficient
C_P	=	Pressure coefficient
M	=	Mach number
N	=	Number of degrees of freedom
P	=	Pressure
Re	=	Reynolds number
η	=	Semispan location
y^+	=	Dimensionless wall-normal distance

*Computational Aerosciences Branch, NAS Division, AIAA Member, leonardo.machado@nasa.gov
†Computational Aerosciences Branch, NAS Division, AIAA Member, timothy.chau@nasa.gov
‡Computational Aerosciences Branch, NAS Division, gaetan.k.kenway@nasa.gov
§Computational Aerosciences Branch, NAS Division, AIAA Member, jared.c.duensing@nasa.gov
¶Computational Aerosciences Branch, NAS Division, AIAA Senior Member, cetin.c.kiris@nasa.gov

Acronyms

BLI	=	Boundary-Layer Ingestion
CFD	=	Computational Fluid Dynamics
DEP	=	Distributed Electric Propulsion
EAP	=	Electrified Aircraft Propulsion
FPR	=	Fan Pressure Ratio
LAVA	=	Launch, Ascent, and Vehicle Aerodynamics
MFR	=	Mass Flow Rate
NLF	=	Natural Laminar Flow
OGV	=	Outlet Guide Vane
PAI	=	Propulsion-Airframe Integration
RANS	=	Reynolds-Averaged Navier Stokes
SUSAN	=	SUbsonic Single Aft eNgine
TCT	=	Tail-Cone Thruster

I. Introduction

A multidisciplinary team at NASA has been researching and developing a new revolutionary hybrid electric aircraft concept called the Subsonic Single Aft Engine (SUSAN) Electrofan [1]. This aircraft aims to target the large regional jet class market with a payload of 180 passengers and a nominal cruise Mach number of 0.785. Among the various technological breakthroughs this concept aims to achieve are included a reduction in the number of hydrocarbon fuel-burning engines from two to one through the use of electrified aircraft propulsion (EAP), distributed electric propulsion (DEP), boundary-layer ingestion (BLI), and natural laminar flow (NLF). These advanced technologies are being integrated onto the SUSAN Electrofan with considerations also toward cost-effectiveness, flight certifiability, and compatibility with existing airport infrastructure.

The overall architecture of the SUSAN Electrofan consists of a tube-and-wing configuration with a hydrocarbon fuel-burning aft fuselage propulsor, or tail-cone thruster (TCT), that produces 35% of the total aircraft thrust while also generating electric power, via a set of generators, to drive wing-mounted electric propulsors which produce the remaining 65% of thrust. Given the decoupling of the power- and thrust-producing elements, this architecture can accommodate a wide range of configurations through various combinations of airframe and propulsion system configurations. Some of these options were investigated by Chau et al. [2], who applied a low-order multidisciplinary design and analysis framework to demonstrate a high potential for improvements to fuel efficiency. The current SUSAN Electrofan concept consists of an aft fuselage BLI engine integrated with a T-tail system and a wing-mounted electric propulsion system, the latter of which is still the subject of investigations by researchers at NASA.

Previous work explored the design and performance of three integrated propulsor concepts developed for BLI, which included overwing, underwing, and trailing-edge configurations [3]. Specifically, the main goal was to investigate the design challenges associated with these novel propulsion-airframe integration (PAI) technologies and the relative benefits of BLI. The overwing configuration was found to be susceptible to shock formation and boundary-layer separation, which reduced both aerodynamic and propulsive efficiency. This was consistent with some of the findings of Lockheed Martin and the Air Force Research Laboratory [4], as well as Lauer and Ansell [5]. The trailing-edge configuration, on the other hand, demonstrated the highest aerodynamic performance with reduced integration penalties given the more decoupled nature of the wing and propulsor designs. However, this concept introduced several system level challenges related to structural design and integration with high-lift devices. Meanwhile, the underwing configuration is in principle compatible with conventional structures, flight control surfaces, and high-lift devices. It was found to offer an acceptable compromise between aerodynamic and propulsive efficiency, even though the boundary layer on the lower surface of the wing can be relatively thinner than that of the wing upper surface [3]. ONERA arrived at a similar conclusion with the DRAGON concept [6, 7], which is a hybrid electric aircraft that features an underwing DEP system with BLI, and blown flaps for enhanced high-lift performance. An analysis of the three configurations was also performed by Lee et al. [8] through internal flow simulations, which indicated shaft power savings of about 13–23% relative to a non-BLI configuration, at least when not considering fan performance penalties due to inlet distortion.

Current research is focused on further maturing the design of the wing-mounted electric propulsion system and on developing a more credible estimate of the potential benefits offered by DEP and BLI. Toward this end, three wing-mounted electric propulsion system configurations are proposed. The first configuration, i.e. Configuration 1, is

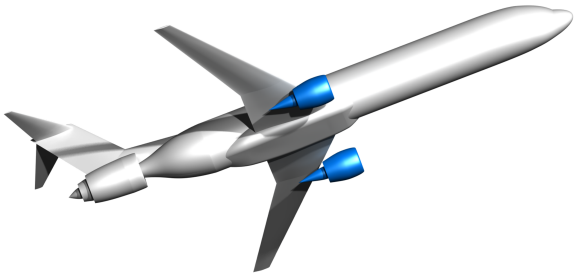

(a) Configuration 1

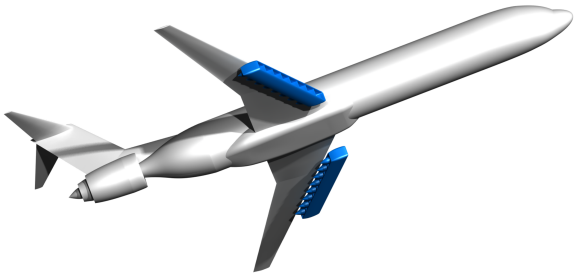

(b) Configuration 2 (DEP)

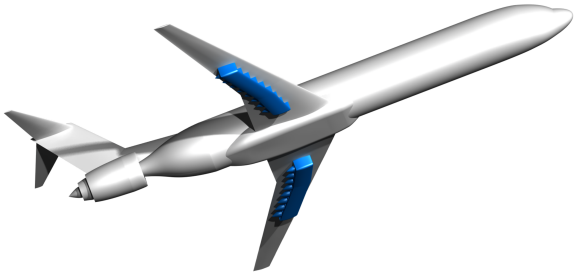

(c) Configuration 3 (DEP + BLI)

Fig. 1 Artistic renderings of the wing-mounted electric propulsor configurations investigated for the SUSAN Electrofan.

shown in Figure 1a and features two underwing podded propulsors developed based on a modern high bypass ratio turbofan. Configuration 1 is regarded as the baseline design. The second configuration, i.e. Configuration 2, is shown in Figure 1b. It introduces the DEP concept with two underwing pylon-mounted arrays of 8 propulsors distributed along the span of each wing for a total of 16 ducted fan units. Despite an increase in wetted area, this concept increases the effective bypass ratio by increasing the fan capture area among several smaller propulsors, thereby lowering the design fan pressure ratio (FPR) of each ducted fan unit [9]. A mail-slot nacelle configuration is adopted in order to reduce flow interference effects across the DEP system, while further reducing individual nacelle wetted area. The third and final configuration, i.e. Configuration 3, is shown in Figure 1c and takes advantage of both DEP and BLI by installing the mail-slot nacelle directly onto the lower surface of the wing. In principle, this improves propulsive efficiency by lowering inlet flow velocity while reducing the wetted area and weight associated with nacelles and pylons [10].

This paper presents a preliminary assessment of the potential relative benefits of DEP by considering Configurations 1 and 2. As a first step, performance requirements for each configuration are defined and initial propulsor concepts are developed. Integration challenges associated with Configuration 2 are then addressed through an iterative design process, starting from a simplified 3-propulsor model before moving to an 8-propulsor concept with sweep and dihedral. These propulsor models are then implemented onto a wing–body model to account for interference effects, and the relative propulsive benefits are assessed.

The paper is organized as follows. The propulsion system design requirements and approach are presented in Section II, while Section III introduces the computational methods and tools used in this work. Sections IV and V present the design processes used to develop baseline propulsor models for Configurations 1 and 2, respectively, while the results of the integrated design analyses are presented and discussed in Section VI. Finally, Section VII concludes the paper by providing a summary of the main findings of the present study, and discusses some of the considerations to be addressed in future works.

II. Propulsion System Design Requirements and Approach

In order to investigate the design and potential benefits offered by the three wing-mounted electric propulsion system configurations described in Section I, representative aircraft models are developed for high-fidelity aeropropulsive

analysis. The main goal is to assess the relative benefits of DEP and BLI, with the present paper focused on the former, namely, a preliminary assessment of Configuration 2 relative to Configuration 1.

For these configurations, the conceptual ducted fan models presented in Sgueglia et al. [11] are used to size the individual propulsors of each propulsion system. Since the focus is on the propulsive benefits of each configuration and because the full SUSAN Electrofan concept has yet to be closed, each propulsion system configuration is assumed to be sized for a total top-of-climb thrust of 51,155 N (11,500 lb) based on a Boeing 737-8-like aircraft [2] at Mach 0.785, an altitude of 11,278 km (37,000 ft), and a Reynolds number of 22.80 million. Although this ignores external airframe drag trades, which are particularly relevant to the evaluation of Configuration 2 due to its higher nacelle wetted area, net thrust calculations are expected to still capture the differences in internal flow wetted area. With an assumed thrust split of 35:65, the wing-mounted electric propulsion systems must generate 33,251 N (7,475 lb) of thrust. The design fan pressure ratios (FPR) of the propulsors used by Configurations 1 and 2 are 1.47 and 1.25, respectively, which provides propulsor mass flow rate (MFR) requirements of 163.02 kg/s and 33.65 kg/s, respectively, based on the low-order models [11]. Configuration 1 features a single fan stage with outlet guide vanes (OGVs) omitted. Configuration 2 includes dual counter-rotating fans to aid in improving low-FPR performance robustness at off-design conditions [8], each of which operate at an FPR of $\sqrt{1.25}$ [3]. An overview of the design requirements is provided in Table 1.

Table 1 Design requirements for each electric propulsion system configuration.

Concept	Configuration 1	Configuration 2
Arrangement	Podded	Distributed
Number of propulsors	2	16
Num. of fans (per propulsor)	1	2
MFR (per propulsor) [kg/s]	163.02	33.65
FPR (per propulsor)	1.47	1.25

Representative models of each propulsion system configuration are then developed, which are successively refined to improve aeropropulsive performance. Given the unique design problem of each configuration, a buildup method is adopted. First, the design and analysis of an isolated propulsor is conducted, followed by a mail-slot design study for Configuration 2. Here, the objective is to define high-fidelity propulsion system models that meet the system-level requirements while minimizing adverse effects. The propulsor models are then integrated with the wing–body model of the current SUSAN Electrofan concept, designed for fully turbulent flow [12], as shown in Figure 2. By including the wing and fuselage, propulsive performance can account for interference effects with the airframe as well as the impact of operating near the on-design angle of attack. Note that although both Configurations 1 and 2 are developed to include pylons, these aircraft components are neglected as higher-order contributions to relative performance.

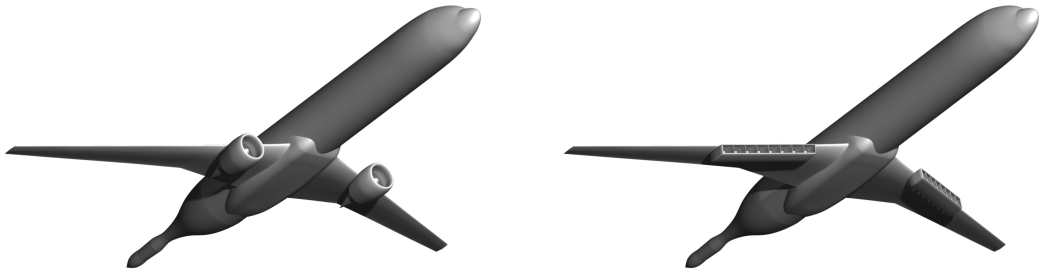

(a) Configuration 1 **(b) Configuration 2 (DEP)**

Fig. 2 Representative aircraft models used to assess the wing-mounted electric propulsion system configurations.

III. Computational Methodology

The Launch, Ascent, and Vehicle Aerodynamics (LAVA) framework [13] is used for the analysis conducted in this work. This software package was developed with the intent of simulating highly complex geometries with flexible mesh paradigm options such as cartesian, unstructured arbitrary polyhedral, and structured curvilinear overset. In this work, flow simulations are performed with structured overset meshes in order to take advantage of their inherent modularity which eases the process of readapting existing meshes when components are swapped or modified. A thorough description of the followed mesh generation procedure can be found in [3]. In order to define appropriate overall mesh resolution guidelines (such as wall normal stretching ratios, leading and trailing edge spacings, etc.), for the design studies that follow, a grid refinement study was conducted and can be found in the Appendix A.

The utilized CFD solver applies a finite difference discretization to the steady-state compressible Reynolds-Averaged Navier Stokes (RANS) equations in strong conservation law form [14], where the convective fluxes of the mean-flow equations are discretized using a second-order accurate modified Roe scheme, with third-order left/right state reconstruction, and a Koren flux limiter [15, 16]. The Spalart-Allmaras (SA) turbulence model [17] with Rotation Curvature [18] and Quadratic Constitutive Relationship corrections [19] (SA-RC-QCR2000) is used for closure with the corresponding convective terms discretized using first-order upwinding.

Propulsion is modeled through an actuator zone methodology [20, 21], where the fan blades are replaced by an axisymmetric fluid volume with an axial thickness equivalent to the blade row. This formulation uses source terms added to the discretized set of equations to model the effect of the propulsion system on the flow and has previously been applied in BLI, and PAI applications [22, 23]. In this study, the actuator zone is applied with a constant radial thrust distribution and is interfaced with a Broyden solver to target a given FPR. Torque effects are neglected as a first-order approximation.

Finally, following common practices, the CFD simulations presented henceforth were run until either the flow equation residuals decreased by six orders of magnitude or the integrated loads presented a standard deviation below one-tenth of a drag count over the last 100 nonlinear iterations.

IV. Configuration 1: Propulsion System Design

This section presents the iterative design process used to develop baseline propulsors for Configuration 1. This involves starting from a reference nacelle and hub geometry, which is then resized and modified to meet the design requirements described in Section II. Design feature modifications are also implemented to address adverse flow features that have a significant impact on drag.

A. Propulsor Design

In order to develop an underwing podded propulsor for Configuration 1, the R4 fan [24] is used as a reference geometry, representing a current generation high-bypass-ratio turbofan that serves as a reasonable starting point. This geometry is modified to include a hub closeout and is scaled to meet the design MFR at an angle of attack of 0°, the design FPR, and the top-of-climb operating conditions. The design and flow features of the initial concept are shown in Figure 3a, where a strong shock is observed at the aft portion of the hub. This is, in part, a consequence of the convergent duct aft of the fan that accelerates the flow to a mass-weighted average Mach number of 1.04 at the nozzle exit, indicating that the flow is choked. The supersonic flow then accelerates over the aft hub to a Mach number upstream of the shock of approximately 1.39, forming a relatively strong shock.

In order to mitigate such flow acceleration, the hub is reshaped and the nozzle exit area is increased by 7.2% as shown in Figure 3b. This results in an exit nozzle Mach number of 0.94 and an increase in MFR of 7.0%. Although a strong shock still persists as a result of the shear layer, the drag coefficient is reduced by 14.3%. With a subsonic Mach number at the exit nozzle achieved, the efforts then shifted to refining the aft hub geometry to better control the pressure gradients contributing to this flow acceleration. A solution was found by extending the aft hub, reducing its slope. The results can be seen in Figure 3c, where the shock strength has been reduced. The upstream Mach number also reduces from 1.44 to 1.37 between iterations 2 and 3, with no major changes in both MFR and C_D noted. The exit nozzle mass-averaged Mach number was also reduced to 0.93.

For the next design iteration, the aft hub was further extended in order to achieve a more gradual pressure recovery at the cost of increased wetted area. The results of this modification are shown in Figure 3d, where the upstream Mach number becomes 1.25 and the exit nozzle Mach number reduces to 0.92. Despite this considerable reduction, the drag coefficient and MFR remain approximately constant. With the returns in drag reduction diminishing, this design iteration was deemed satisfactory.

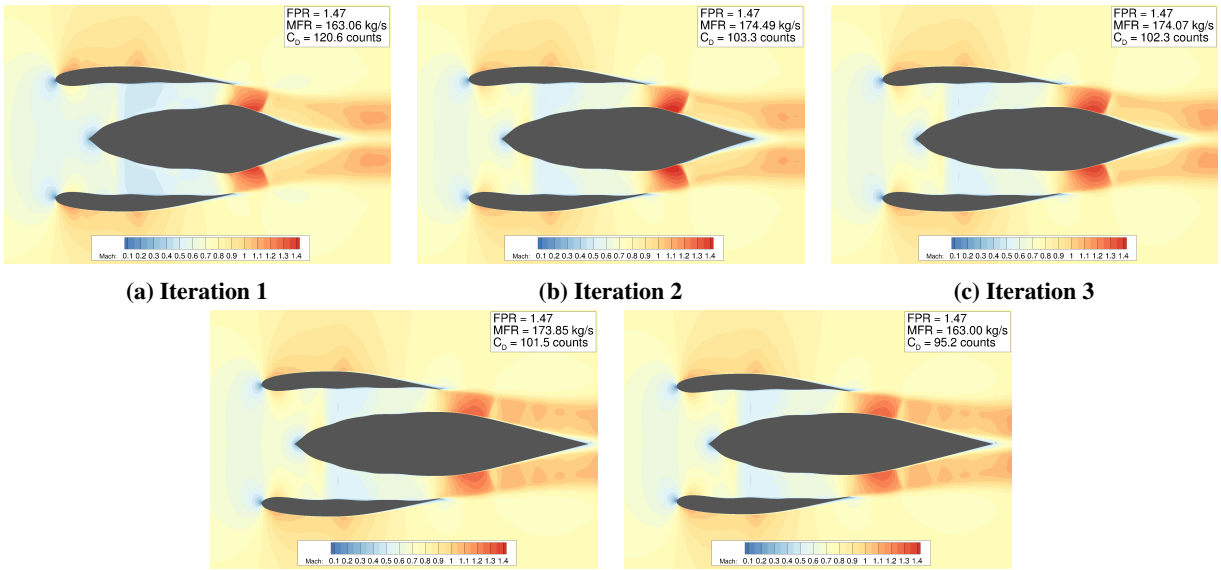

(a) Iteration 1 **(b) Iteration 2** **(c) Iteration 3**

(d) Iteration 4 **(e) Iteration 5**

Fig. 3 Configuration 1: Propulsor design evolution.

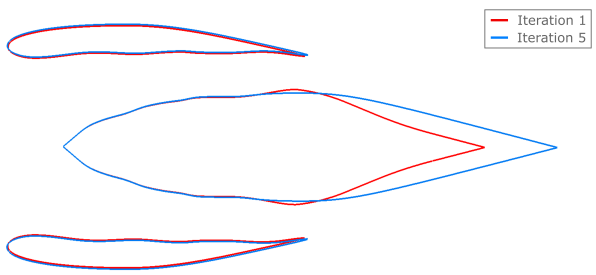

Fig. 4 Configuration 1: Comparison between initial and final propulsor designs.

As a final step, the nacelle and hub design are downsized in order to adjust the MFR to meet the requirement, assuming proportionality between the inlet area and mass flow rate. This iteration is shown in Figure 3e. Similar flow features are observed, where a 6.2% reduction in C_D is achieved through a reduction in wetted area. Nevertheless, a fan face Mach number of 0.74 is observed, which is in part responsible for the moderate shocks forming over the aft hub. This can be addressed by modifying the diffuser length, nacelle droop angle, or nacelle highlight area, as a few examples. As a representative geometry, however, this design iteration is considered adequate in terms of feasibility and aerodynamic performance. Figure 4 shows a comparison between the initial and final design iterations.

V. Configuration 2: Propulsion System Design

For Configuration 2, a mail-slot nacelle concept is developed. This involved the development of a single propulsor design that meets system-level requirements, which is then integrated into a mail-slot nacelle with splitters. The design is simplified, featuring rectangular ducts similar to the representative models investigated by Wick et al. [4]. By introducing source terms to the momentum and energy equations, however, the actuator zones offer an improved level of fidelity over mass flow rate boundary faces, and result in a more credible estimate of the potential benefits offered by novel propulsion concepts such as DEP.

A. Propulsor Design

The first iteration of the propulsor model is based on previous work done by Lee et al. [8], which focused on developing an initial electric propulsor design for the SUSAN Electrofan. This model is then modified to address adverse effects, such as strong external nacelle shocks, while maintaining the design FPR and MFR. From Figure 5a, a relatively strong shock can be seen over the lip of the nacelle, which results from its small leading-edge radius. This comes from a rough initial design where the focus was on developing an internal flow path that was originally suitable for BLI concepts.

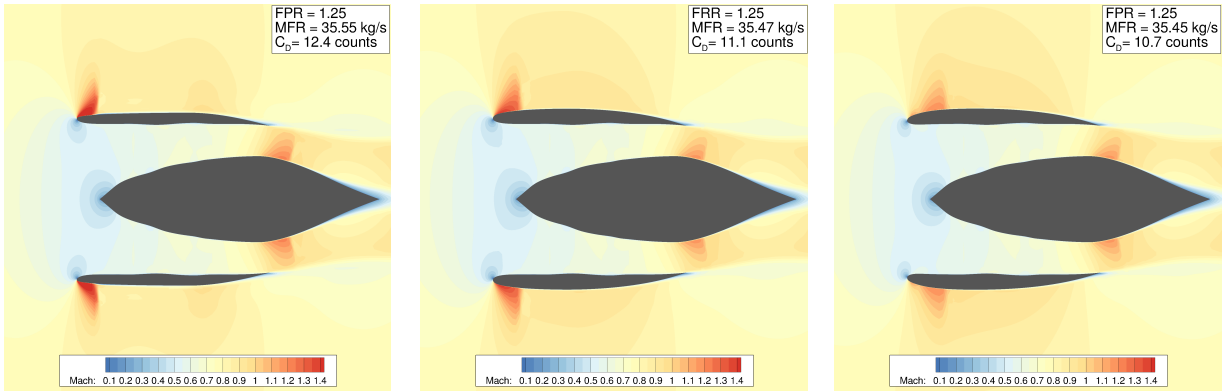

(a) Iteration 1 **(b) Iteration 2** **(c) Iteration 3**

Fig. 5 Configuration 2: Propulsor design evolution.

As a first step, a new external profile is developed following the approach presented by Peters et al. [25] using a NASA SC(2)-0710 airfoil profile. As shown in Figure 5b, the shock strength has been reduced, corresponding to a decrease in C_D of 10.4%. The aft hub shock has also diminished, consistent with the reduced suction peak.

In order to further reduce the shock strength over the nacelle, modifications to the droop angle are introduced to better align the nacelle camber line with the incoming stagnation point streamline. This slows flow expansion as the flow rounds the leading edge. The success of this change can be seen in Figure 5c, which corresponds to a further reduction in C_D of 3.7%. Pressure distributions over the centerline nacelle profile of each design iteration are shown in Figure 6, which highlights the progression of nacelle lip shock strength reduction. Figure 7 provides a comparison between the initial and final designs.

B. Mail-Slot Nacelle Design

With an initial ducted fan propulsor design defined for a DEP system that meets the system-level requirements, the next step was to extend the concept to a mail-slot nacelle configuration. Toward this end, a representative model is developed based on the NASA N3-X [26, 27] and the concepts investigated by Wick et al. [4]. Given that the primary objective of the present work is to assess the relative benefits offered by DEP, the development of the mail-slot nacelle configuration assumes a number of geometry simplifications. For example, the internal flow paths are modeled as rectangular ducts that are created by extruding the baseline nacelle and hub profiles, following the work of Wick et al. [4]. The ducted fan units are separated by splitters and the core duct profiles are maintained at 0°, 90°, 180°, and 270°. In contrast to the concepts of Wick et al. [4], the hubs remain axisymmetric, with the actuator zones idealized and stretched over the core ducts to maintain a more similar gross thrust per unit capture area as that of a circular duct with a circular actuator zone.

One of the key challenges in developing a mail-slot nacelle in an underwing arrangement at transonic operating conditions is the need for relatively high sweep angles to avoid the formation of upper surface shocks, especially at nonzero angles of attack. Although the external nacelle profile can be lofted to achieve this, the same cannot be done with the internal nacelle profile due to the core ducts, which must remain unswept and oriented about the hub. In order to avoid a clipping of these core regions, the nacelle inlet and exit regions must be elongated proportionately with sweep. Therefore, the baseline nacelle and hub profiles are extended to accommodate a 29.0 degree leading-edge sweep, with the hub length also increased to include a constant area region toward the exit nozzle that prevents a further acceleration of the flow. A dihedral angle of 3.74 degrees is also considered based on a local averaging of the wing dihedral. This is

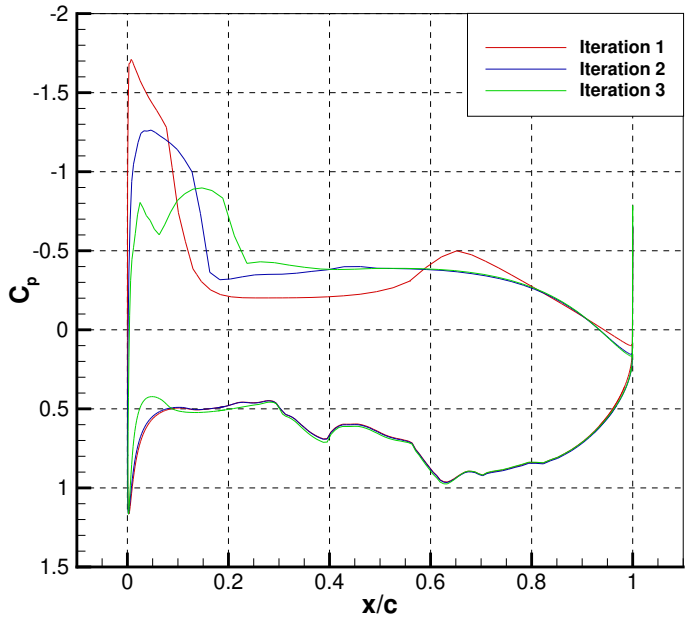

Fig. 6 Nacelle surface pressure distributions.

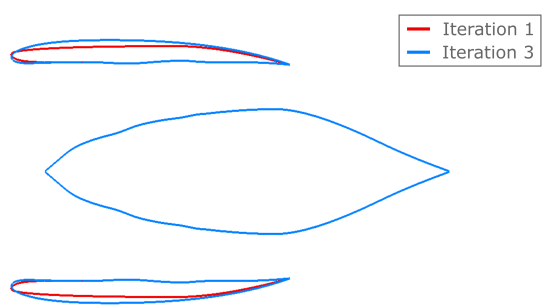

Fig. 7 Configuration 2: Comparison between preliminary initial and final propulsor designs.

realized through a rotation of the mail-slot nacelle configuration to avoid a vertical staggering of the ducted fan units. A comparison between the cross-sections of the isolated propulsor, presented in the previous section, and of the modified design developed for integration with the mail-slot is presented in Figure 8.

Figure 9 shows the ducted fan propulsor design created from the modified nacelle and hub profiles, which is used to assess the impact that these changes have on the flow and aeropropulsive performance. The geometry is also scaled down to maintain a similar capture area when moving to the rectangular cross-sections of the mail-slot nacelle configuration. Results are shown in Figure 10 where centerline Mach number contours are illustrated at an FPR of 1.25. A strong shock is observed at the exit nozzle with a modest region of flow separation downstream along the hub. These changes decrease the mass flow rate and drag coefficient to 24.28 kg/s and 5.9 counts, respectively, with the former largely due to scaling.

The next step toward developing a mail-slot nacelle configuration is to develop a simplified 3-propulsor model, as shown in Figure 11. This represents the simplest version of a mail-slot nacelle that does not include sweep and dihedral and is used for preliminary investigations of the integration effects. An extension of the splitter was found to be necessary in order to avoid premature flow expansion originating at the $z = 0$ plane which lead to severe interference

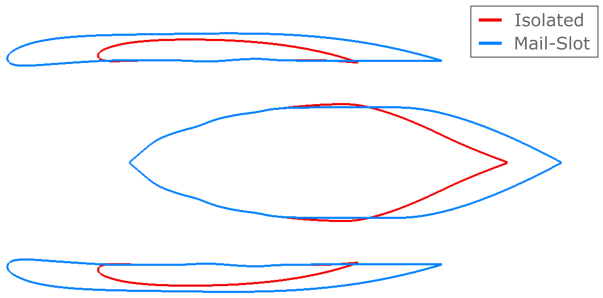

Fig. 8 Configuration 2: Comparison between the initial propulsor design and the modified design developed for integration into a high-sweep mail-slot nacelle.

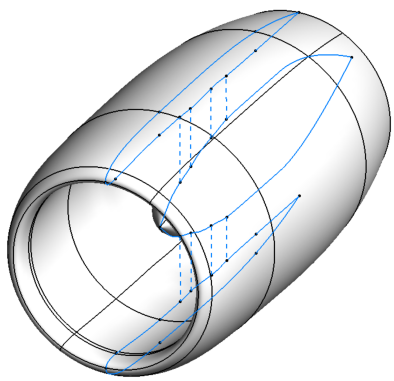

Fig. 9 Configuration 2: Ducted fan propulsor.

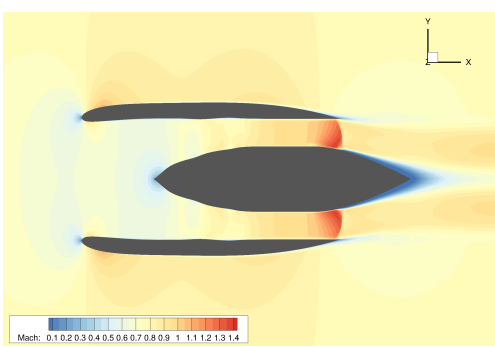

Fig. 10 Configuration 2: Mach number contours at the centerline of the ducted fan propulsor design used to accommodate a high-sweep mail-slot nacelle configuration.

effects between adjacent propulsors. In effect, the splitter extension maintains the constant area region over the exit region of the core duct, delaying the area divergence that comes from the aft hub and splitter closeouts. Figure 12 shows the Mach contours at $z = 0$ at an FPR of 1.25. Due to the reduced levels of diffusion over the rectangular nacelle inlet, the fan face Mach also increases substantially, which contributes to the supersonic diffusion seen toward the exit nozzle. The average propulsor mass flow rate is 33.35 kg/s, while the average drag coefficient is reduced by 6% relative to the single propulsor. This is likely due to the reduced wetted area provided by the distributed propulsor integration.

Finally, the 3-propulsor concept is extended to the 8-propulsor mail-slot nacelle configuration, where nacelle sweep and dihedral are introduced. In order to accommodate sweep, the core ducts are staggered in the streamwise direction

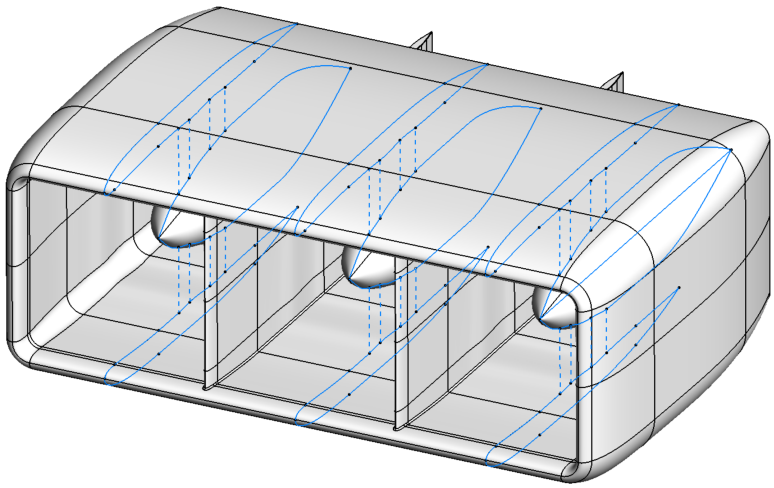

Fig. 11 Configuration 2: 3-propulsor mail-slot nacelle concept.

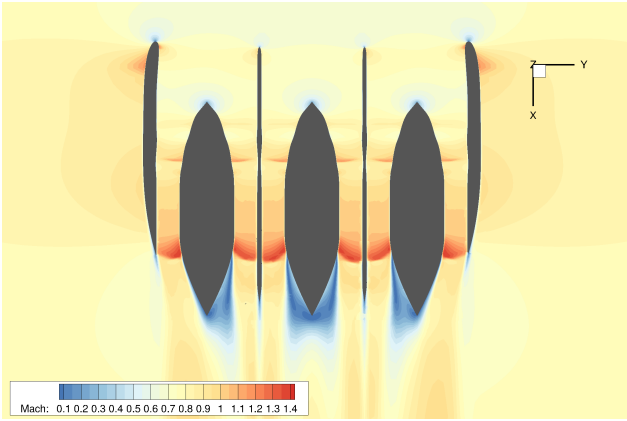

Fig. 12 Configuration 2: Mach number contours at the $z = 0$ plane of the 3-propulsor mail-slot nacelle concept.

along the span. The external nacelle profile is lofted in the spanwise direction, maintaining smooth lower and upper surfaces that are less susceptible to wave drag. The internal nacelle profiles, at both the inlet and exit, are re-lofted in the spanwise direction across a given ducted fan unit to maintain start and end core duct boundaries that are aligned with the yz-plane. This can lead to non-uniform flow features at the start of the core duct since the nacelle inlet is much longer inboard than it is outboard, but care is taken to maintain a constant nacelle diffuser area ratio from the nacelle highlight to the fan face. Since the nacelle exit is designed intentionally with a prolonged constant area region, these non-uniform effects are less likely to originate downstream of the core duct. To maintain a smooth and watertight geometry, the splitters are carefully positioned to embed the geometric discontinuities between two adjacent ducted fan units.

Figure 13 shows the representative model for the 8-propulsor mail-slot nacelle configuration. Note that the geometry is rotated along the x-axis to accommodate dihedral. Figure 14 presents Mach contours at the local $z = 0$ plane, where the strength of shock surfaces present within the internal flow paths have increased in magnitude. This is likely a consequence of cross-flow effects introduced by sweep, which lead to slightly higher fan face Mach numbers toward the outboard. These cross-flow effects also increase the strength of shocks present in the outboard duct of each propulsor, which leads to regions of shock-induced flow separation over the aft hub, similar to those encountered by ONERA [7]. Nonetheless, the concept experiences a comparable average drag coefficient and mass flow rate relative to the 3-propulsor configuration.

Table 2 presents a comparison between the 1-propulsor, 3-propulsor, and 8-propulsor mail-slot nacelle configurations. Here, it can be seen that the average propulsor drag coefficient is similar between the 3-propulsor and 8-propulsor

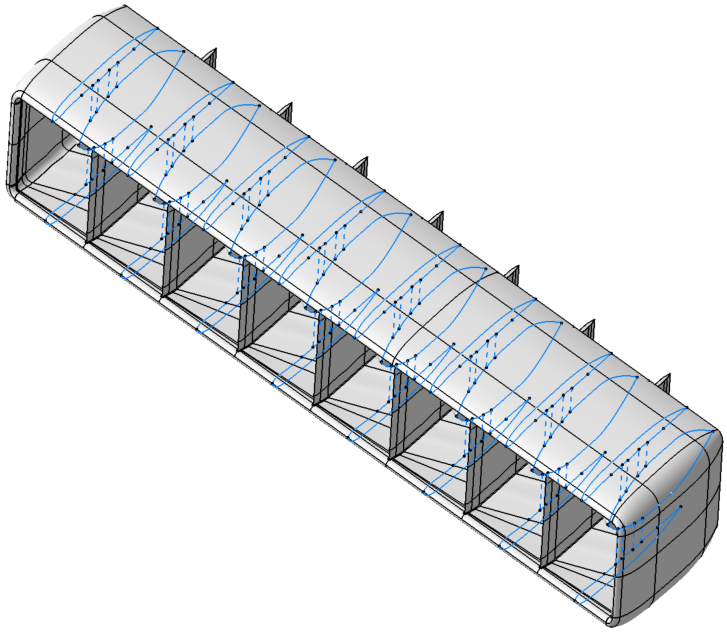

Fig. 13 Configuration 2: 8-propulsor mail-slot nacelle concept with sweep and dihedral.

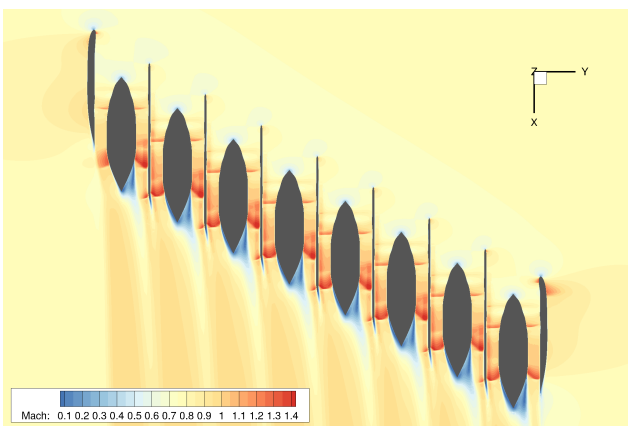

Fig. 14 Configuration 2: Mach number contours at the local $z = 0$ plane of the 8-propulsor mail-slot nacelle concept.

configurations, and is lower than that of the 1-propulsor configuration despite the higher levels of adverse effects. This is largely due to the savings in wetted area that are gained by merging adjacent nacelles in a mail-slot arrangement.

VI. Integrated Design Analysis

In order to assess the potential relative benefits of DEP, the representative propulsion systems presented in Sections IV and V are integrated onto a clean wing–body model of the SUSAN Electrofan. The aircraft concepts are then trimmed with respect to the angle of attack with propulsion systems active to meet a design lift coefficient of 0.50. The relative benefit of DEP is then given by comparing the shaft power [11, 28] required by each configuration to meet the same net thrust at the design operating conditions.

In principle, each propulsion system should produce the same net thrust at the design operating conditions based on the sizing process described in Section II. However, since this was done through low-order models, discrepancies can be

Table 2 Mail-slot configuration results.

Configuration	1-Propulsor	3-Propulsor	8-Propulsor
Angle of attack [°]	0.000	0.000	0.000
FPR (per propulsor)	1.25	1.25	1.25
MFR (per propulsor) [kg/s]	24.28	33.35	33.65
C_D (per propulsor) [counts]	5.9	5.5	5.5
C_D (total) [counts]	5.9	16.6	44.0

Table 3 A comparison of propulsive efficiency for the wing-mounted propulsion system configurations.

Concept	Wing-Body	Configuration 1	Configuration 2
Angle of attack [°]	2.102	2.356	2.347
Lift coefficient	0.50	0.50	0.50
FPR (per propulsor)	–	1.45	1.25
MFR (per propulsor) [kg/s]	–	160.20	33.64
MFR (total) [kg/s]	–	320.41	538.24
Shaft power (per propulsor) [MW]	–	4.626	0.571
Shaft power (total) [MW]	–	9.252	9.131

expected when compared to the high-fidelity designs and simulation results. Differences also arise when accounting for the changes to the operating conditions that come from trimming the angles of attack. Although the errors in net thrust are only on the order of 3–5%, a fair comparison requires that each concept provide the same net thrust. Therefore, the design FPR of Configuration 1 is reduced from 1.47 to 1.45 to meet the net thrust of Configuration 2, since increasing the design FPR of Configuration 2 instead would move it beyond its operating envelope.

Table 3 provides a summary of the results obtained from the CFD simulations. One of the most significant advantages of DEP comes from its higher capture area, which translates to a higher mass flow rate per unit thrust. This can be seen in the mass flow rate of Configuration 2, which is 1.7 times that of Configuration 1. However, although this translates to a much lower change in enthalpy across each individual propulsor, the savings in shaft power offered by Configuration 2 is only 1.3% relative to Configuration 1. This is in part due to the internal wetted area penalties associated with having 16 ducted fan units, which overcome the benefits of reduced work.

In order to gain further insight, CFD simulations of the propulsion system configurations are performed with power off at constant angle of attack. Table 4 provides a comparison between the power-on and power-off cases for each configuration. Here, it can be seen that the total drag difference is largely due to the difference in propulsor drag since the changes in airframe drag (i.e. wing and fuselage) are minimal. For Configuration 2, this difference is slightly larger because of an increase in lift with power off, leading to a small drag rise that is lift-induced. Of particular interest, however, is the relative change in propulsor drag that comes from producing thrust, namely, thrust-induced drag. Note that the drag presented here is not discounted by the internal flow drag that is normally accounted for in net thrust. For Configuration 1, the thrust-induced drag increment is +155.7 counts, which is an increase of 4–5 times when compared to that of Configuration 2 at +42.3 counts or 1.5–2 times. This leads to a total drag savings of 22.2% for Configuration 2 relative to Configuration 1.

Although this difference is insufficient to translate to a more substantial benefit in terms of total shaft power, these comparisons suggest that the DEP system has a high potential that has not yet been realized. Specifically, if the two configurations are trimmed with respect to thrust and drag, for example, the difference in drag between Configurations 1 and 2 is likely to widen due to reductions in thrust-induced drag, leading to more significant savings in shaft power. In effect, the small relative benefit of Configuration 2 is the result of an oversized propulsion system that comes as a consequence of the prescribed top-of-climb thrust target, which was a system-level assumption. Leveraging the reductions in thrust-induced drag offered by Configuration 2 can lead to a reduced net thrust requirement, which translates to a downsizing in the overall propulsion system and a potential decrease in the design FPR.

Table 4 A comparison of drag for the wing-mounted propulsion system configurations.

Concept	Configuration 1			Configuration 2		
Mode	Power Off	Power On	ΔC_D	Power Off	Power On	ΔC_D
Angle of attack [°]	2.356	2.356	–	2.347	2.347	–
Lift coefficient	0.51	0.50	–	0.52	0.50	–
FPR (per propulsor)	1.00	1.45	–	1.00	1.25	–
Airframe C_D[a] [counts]	202.0	202.8	+0.8	219.5	213.9	−5.6
Propulsor C_D[b] [counts]	41.8	197.5	+155.7	55.5	97.8	+42.3
Total C_D [counts]	243.8	400.4	+156.6	275.0	311.7	+36.7

[a]Includes wing and fuselage.

[b]Includes nacelle and hub.

With regard to the aerodynamic impact of the propulsion system configurations on the wing–body model, Table 3 indicates that Configuration 1 experiences higher levels of wing flow interference when compared to Configuration 2, as evidenced by its slightly larger trimmed angle of attack. This can be seen from the surface pressure contours and distributions shown in Figures 15 and 16, where at 15% semispan a relatively strong upper surface shock is present, and at 30% semispan, a decrease in local pressure can be seen, which corresponds to the transonic channel effect. It should be noted, however, that the airframe drag is higher for Configuration 2 when compared to Configuration 1. This appears to be caused by modest interference effects on the pressure distributions of the wing that are present over the extent of the mail-slot nacelle, leading to a higher integrated drag change when compared to the more local adverse effects of the podded propulsor configuration. Although a redesign of the wing–body model is warranted in order to mitigate these effects in the presence of the propulsion system, their impact on the integrated loads is relatively modest and is assumed to not largely affect the conclusions of this work.

VII. Conclusions

This paper presents a preliminary assessment of the potential relative benefits of DEP for the wing-mounted electric propulsion system of the SUSAN Electrofan, as well as an initial exploration of the DEP system design space. In order to obtain an estimate of the relative benefit offered by DEP, representative models are developed for two propulsion system configurations. Utilizing Configuration 1 as a baseline with two underwing-mounted podded propulsors, and comparing it with Configuration 2, which represents the DEP concept with 16 propulsors in a mail-slot nacelle, the relative benefits of this technology could be assessed.

Propulsion system concepts are first developed to meet an assumed system-level top-of-climb net thrust requirement. These are then used to develop high-fidelity models of each propulsion system configuration, with a focus on achieving designs that satisfy the net thrust requirement at their design FPRs and MFRs, while minimizing adverse flow features that impact drag. For Configuration 2, special attention is made toward accommodating a mail-slot nacelle concept with high sweep and splitters, which involves unique modifications such as elongated nacelle inlets and exit regions.

The propulsion systems are then integrated onto the wing–body model of the SUSAN Electrofan, with the aircraft configurations trimmed to meet the design lift coefficient in order to study first-order interference effects on both aerodynamics and propulsion. Results indicate that Configuration 2 provides a 1.3% savings in shaft power when compared to Configuration 1, due to its higher capture area and lower design fan pressure ratios. A comparison between powered and unpowered simulations, however, suggests that DEP has more to offer due to its much lower thrust-induced drag. For instance, Configuration 2 offers a total drag savings of 22.2% relative to Configuration 1 at the same net thrust, which primarily comes from a reduction in thrust-induced drag of 72.8%. Although this was insufficient to translate to a more substantial shaft power saving when summing the contributions from each individual ducted fan unit, these results suggest that a more significant benefit can be achieved if the net thrust requirement is adjusted based on the external drag of each resulting aircraft configuration.

Future work will address this by relaxing the assumption of equal system-level net thrust, and accounting for the dependence of simulated aircraft drag on top-of-climb thrust. A wing redesign will also be included to account for the PAI effects, which will be especially relevant when including an assessment of the relative benefits offered by DEP and

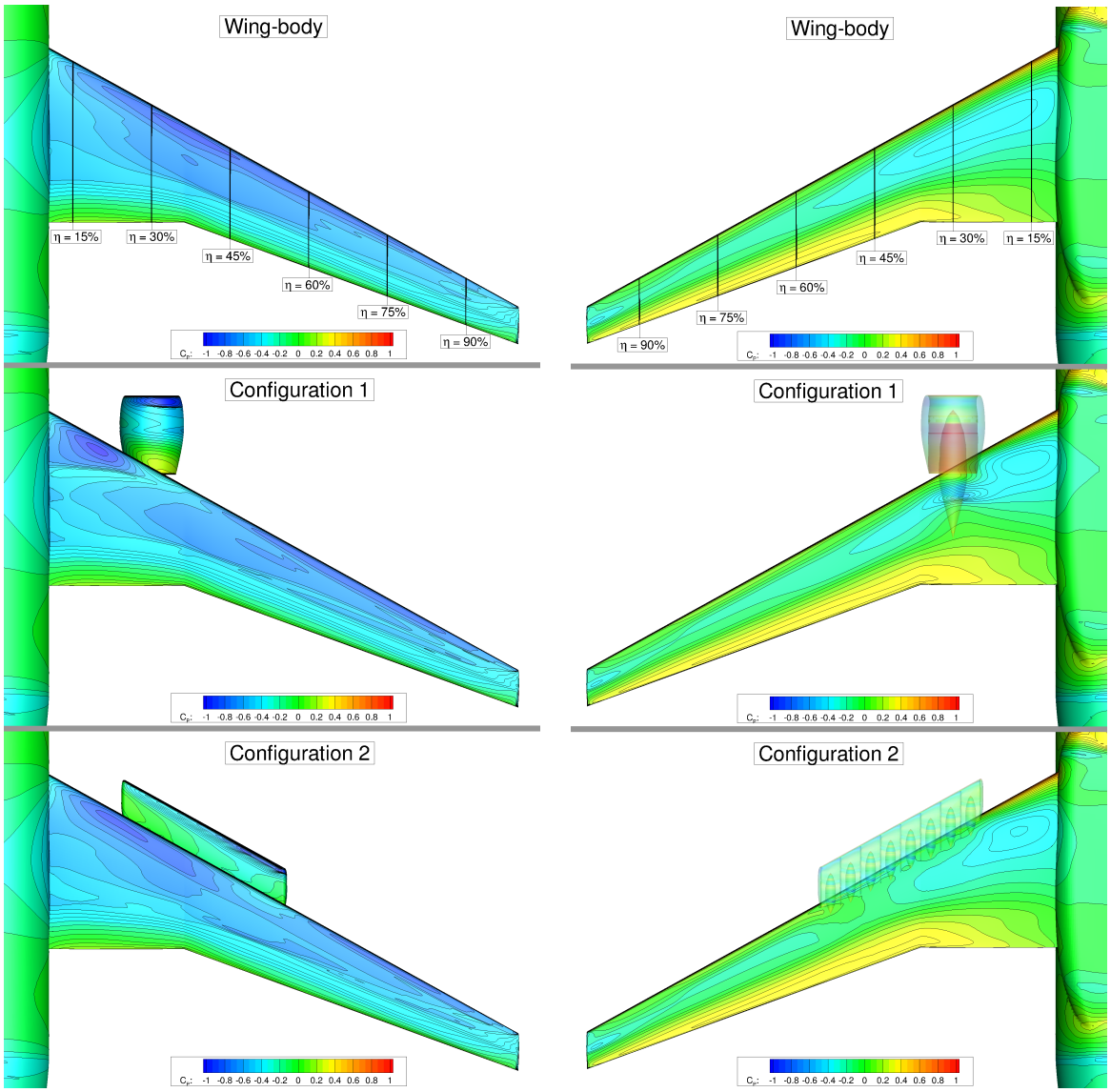

(a) Suction side **(b) Pressure side**

Fig. 15 Pressure coefficient contours.

BLI, as per Configuration 3. Once the relative benefits have been established and a propulsion system configuration has been selected for the SUSAN Electrofan, a more detailed design of the wing-mounted propulsion system will be performed. This will include geometry modifications to the mail-slot nacelle concepts in order to incorporate circular ducts over the core region of each propulsor unit, and a more realistic design of the splitters and their extensions.

Acknowledgments

This work was sponsored by the Convergent Aeronautics Solutions (CAS) project, which is part of the Transformational Aeronautics Concepts Program (TACP) in the NASA Aeronautics Mission Directorate (ARMD). The authors would like to gratefully acknowledge Michael Piotrowski, Jeffrey Housman, Gerrit Stich, and the rest of the LAVA team for helpful advice and feedback. We would also like to leave a special note to Michelle Banchy, Brett Hiller, and Richard Campbell, for providing the fully turbulent wing design used in this work. The authors also acknowledge Ralph Jansen, Mark Turner, and the rest of the SUSAN team for valuable discussions, and James Koch and Daniel Maldonado for

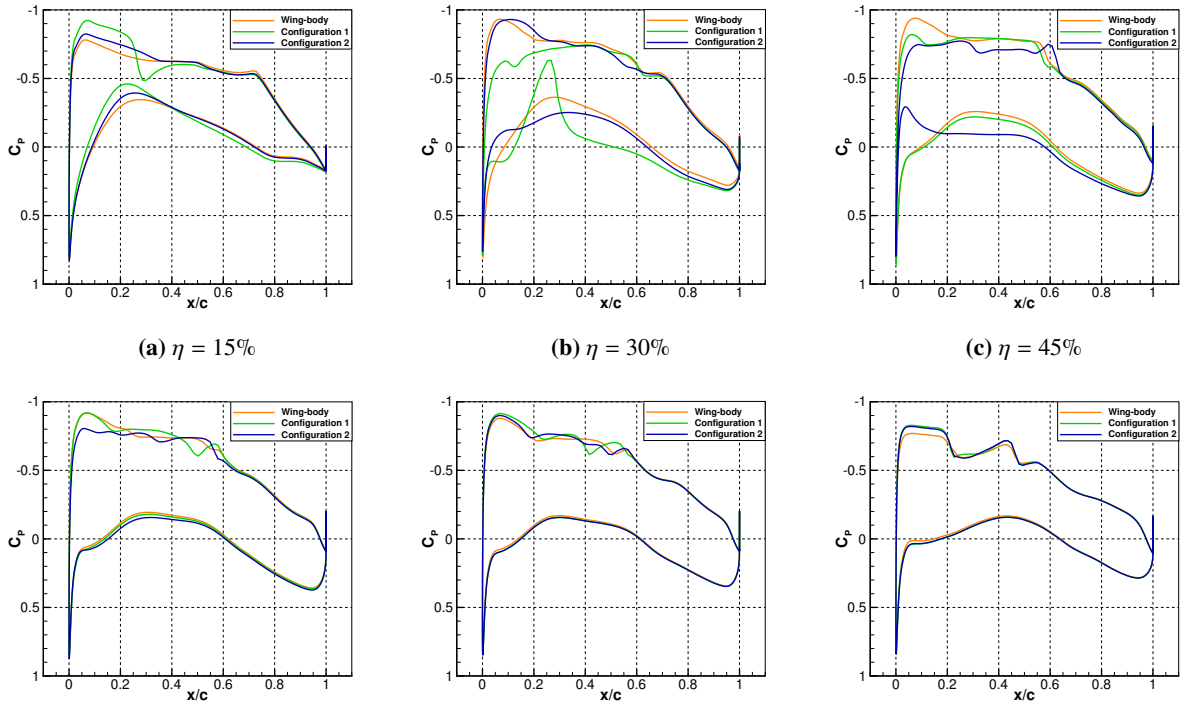

(a) η = 15%

(b) η = 30%

(c) η = 45%

(d) η = 60%

(e) η = 75%

(f) η = 90%

Fig. 16 Surface pressure distributions at various spanwise locations.

internal review. Computational resources were provided by the NASA High-End Computing (HEC) Program through the NASA Advanced Supercomputing (NAS) Division at Ames Research Center.

References

[1] Jansen, R. H., Kiris, C. C., Chau, T., Kenway, G. K. W., Machado, L. G., Duensing, J. C., Mirhashemi, A., Haglage, J. M., Dever, T. P., Chapman, J. W., French, B. D., Goodnight, T. W., Miller, L. R., Litt, J. S., Denham, C. L., Lynde, M., Campbell, R., Hiller, B., and Heersema, N., "Subsonic Single Aft Engine (SUSAN) Transport Aircraft Concept and Trade Space Exploration," *AIAA SciTech Forum*, AIAA 2022-2179, San Diego, CA, January 2022. https://doi.org/10.2514/6.2022-2179.

[2] Chau, T., Kenway, G. K. W., and Kiris, C. C., "Conceptual Exploration of Aircraft Configurations for the SUSAN Electrofan," *AIAA SciTech Forum*, AIAA 2022-2181, San Diego, CA, January 2022. https://doi.org/10.2514/6.2022-2181.

[3] Machado, L. M. G., Chau, T., Kenway, G. K. W., Duensing, J., and Kiris, C. C., "High Fidelity Computational Analysis and Optimization of the SUSAN Electrofan Concept," *AIAA SciTech Forum and Exposition*, AIAA 2022-2304, San Diego, CA, January 2022. https://doi.org/10.2514/6.2022-2304.

[4] Wick, A. T., Hooker, J. R., and Hardin, C. J., "Integrated Aerodynamic Benefits of Distributed Propulsion," *AIAA SciTech Forum*, AIAA 2015-1500, Kissimmee, FL, January 2015. https://doi.org/10.2514/6.2015-1500.

[5] Lauer, M. G., and Ansell, P. J., "Aerodynamic Shape Optimization of a Transonic, Propulsion-Airframe-Integrated Airfoil System," *AIAA Aviation Forum*, AIAA 2022-3662, Chicago, IL, June 2022. https://doi.org/10.2514/6.2022-3662.

[6] Schmollgruber, P., Döll, C., Hermetz, J., Liaboeuf, R., Ridel, M., Atinault, I. C. O., François, C., and Paluch, B., "Multidisciplinary Design and Performance of the ONERA Hybrid Electric Distributed Propulsion Concept (DRAGON)," *AIAA SciTech Forum*, AIAA 2020-0501, San Diego, CA, January 2019. https://doi.org/10.2514/6.2019-1585.

[7] Schmollgruber, P., Donjat, D., Ridel, M., Cafarelli, I., Atinault, O., François, C., and Paluch, B., "Multidisciplinary Design and Performance of the ONERA Hybrid Electric Distributed Propulsion Concept (DRAGON)," *AIAA SciTech Forum*, AIAA 2020-0501, Orlando, FL, January 2020. https://doi.org/10.2514/6.2020-0501.

[8] Lee, B. J., and Liou, M.-F., "Conceptual Design of Propulsors for the SUSAN Electrofan Aircraft," *AIAA SciTech Forum and Exposition*, AIAA 2022-2305, San Diego, CA, January 2022. https://doi.org/10.2514/6.2022-2305.

[9] Kim, H. D., Perry, A. T., and Ansell, P. J., "A Review of Distributed Electric Propulsion Concepts for Air Vehicle Technology," *AIAA Propulsion and Energy Forum*, AIAA 2018-4998, Cincinnati, OH, July 2018. https://doi.org/0.2514/6.2018-4998.

[10] Hall, D. K., Huang, A. C., Uranga, A., Greitzer, E. M., Drela, M., and Sato, S., "Boundary Layer Ingestion Propulsion Benefit for Transport Aircraft," *Journal of Propulsion and Power*, Vol. 33, No. 5, 2017, pp. 1118–1129. https://doi.org/10.2514/1.B36321.

[11] Sgueglia, A., Schmollgruber, P., Bartoli, N., Atinault, O., Benard, E., and Morlier, J., "Exploration and Sizing of a Large Passenger Aircraft with Distributed Ducted Electric Fans," *AIAA SciTech Forum*, AIAA 2018-1745, Kissimmee, FL, January 2018. https://doi.org/10.2514/6.2018-1745.

[12] Lynde, M. N., Campbell, R., and Hiller, B. R., "A Design Exploration of Natural Laminar Flow Applications for the SUSAN Electrofan Concept," *AIAA SciTech Forum*, AIAA 2022-2303, San Diego, CA, January 2022. https://doi.org/10.2514/6.2022-2303.

[13] Kiris, C. C., Housman, J. A., Barad, M. F., Brehm, C., Sozer, E., and Moini-Yekta, S., "Computational Framework for Launch, Ascent, and Vehicle Aerodynamics (LAVA)," *Aerospace Science and Technology*, Vol. 55, No. 1, 2016, pp. 189–219. https://doi.org/10.1016/j.ast.2016.05.008.

[14] Vinokur, M., "Conservation Equations of Gasdynamics in Curvilinear Coordinate Systems," *Journal of Computational Physics*, Vol. 14, No. 2, 1974, pp. 105–125. https://doi.org/10.1016/0021-9991(74)90008-4.

[15] Housman, J. A., Kiris, C. C., and Hafez, M. M., "Time-Derivative Preconditioning Methods for Multicomponent Flows - Part I: Riemann Problems," *Journal of Applied Mechanics*, Vol. 76, No. 2, 2009, pp. 1–13. https://doi.org/10.1115/1.3072905.

[16] Housman, J. A., Kiris, C. C., and Hafez, M. M., "Time-Derivative Preconditioning Methods for Multicomponent Flows—Part II: Two-Dimensional Applications," *Journal of Applied Mechanics*, Vol. 76, No. 3, 2009, pp. 1–12. https://doi.org/10.1115/1.3086592.

[17] Spalart, P. R., and Allmaras, S. R., "A One-Equation Turbulence Model for Aerodynamic Flows," *30th AIAA Aerospace Sciences Meeting and Exhibit*, AIAA 92-0439, Reno, Nevada, January 1992. https://doi.org/10.2514/6.1992-439.

[18] Shur, M. L., Strelets, M. K., Travin, A. K., and Spalart, P. R., "Turbulence Modeling in Rotating and Curved Channels: Assessing the Spalart-Shur Correction," *AIAA Journal*, Vol. 38, No. 5, 2000, pp. 784–792. https://doi.org/10.2514/2.1058.

[19] Spalart, P. R., "Strategies for Turbulence Modelling and Simulations," *International Journal of Heat and Fluid Flow*, Vol. 21, No. 3, 2000, pp. 252–263. https://doi.org/10.1016/S0142-727X(00)00007-2.

[20] Svenning, E., "Implementation of an Actuator Disk in OpenFOAM," Tech. rep., Chalmers University of Technology, 2010.

[21] Stich, G.-D., Fernandes, L. S., Duensing, J. C., Housman, J. A., Kenway, G. K. W., and Kiris, C. C., "Validation of Actuator Disk, Actuator Line and Sliding Mesh Methods within the LAVA Solver," *International Conference on Computational Fluid Dynamics 11*, ICCFD, Maui, HI, July 2022.

[22] Hall, D. K., Greitzer, E. M., and Tan, C. S., "Analysis of Fan Stage Conceptual Design Attributes for Boundary Layer Ingestion," *Journal of Turbomachinery*, Vol. 139, No. 7, 2017, pp. 1–10. https://doi.org/10.1115/1.4035631.

[23] Fernandes, L. S., Machado, L. G., Duensing, J. C., and Kiris, C. C., "Computational Aerodynamics Analysis in Support of the CRM Tail Cone Thruster Configuration Wind Tunnel Test," *AIAA SciTech Forum*, AIAA 2022-1171, San Diego, CA, January 2022. https://doi.org/10.2514/6.2022-1171.

[24] Van Zante, D. E., Podboy, G. G., Miller, C. J., and Thorp, S. A., "Testing and Performance Verification of a High Bypass Ratio Turbofan Rotor in an Internal Flow Component Test Facility," Tech. rep., NASA, 2009. NASA/TM 2009-215661.

[25] Peters, A., Spakovszky, Z. S., Lord, W. K., and Rose, B., "Ultrashort Nacelles for Low Fan Pressure Ratio Propulsors," *Journal of Turbomachinery*, Vol. 137, No. 2, 2015, pp. 1–14. https://doi.org/10.1115/1.4028235.

[26] Kim, H., Lious, M.-F., and Liou, M.-S., "Mail-Slot Nacelle Shape Design for N3-X Hybrid Wing-Body Configuration," *AIAA Propulsion and Power Forum*, AIAA 2015-3805, Orlando, FL, July 2015. https://doi.org/10.2514/6.2015-3805.

[27] Lee, B. J., Liou, M.-F., and Kim, H., "Design of Distributed Mail-Slot Propulsion System on a Hybrid Wingbody Aircraft," *AIAA Aviation Forum*, AIAA 2018, Atlanta, GA, June 2018.

[28] Gray, J. S., Mader, C. A., Kenway, G. K. W., and Martins, J. R. R. A., "Modeling Boundary Layer Ingestion Using a Coupled Aeropropulsive Analysis," *Journal of Aircraft*, Vol. 55, No. 3, 2018, pp. 1191–1199. https://doi.org/10.2514/1.C034601.

[29] Tinoco, E. N., Brodersen, O. P., Keye, S., Laflin, K. R., Feltrop, E., Vassberg, J. C., Mani, M., Rider, B., Wahls, R. A., Morrison, J. H., Hue, D., Roy, C. J., Mavriplis, D. J., and Murayama, M., "Summary Data from the Sixth AIAA CFD Drag Prediction Workshop: CRM Cases," *Journal of Aircraft*, Vol. 55, No. 4, 2018, pp. 1352–1379. https://doi.org/10.2514/1.C034409.

Appendix A. Grid Refinement Studies

A grid refinement study with the wing–body model of the SUSAN Electrofan was conducted at the flow condition described in Section II and a lift coefficient of 0.50, to establish an overall adequate mesh resolution for the design studies. This assumes the dominant aerodynamic effects, including shocks, behave similarly between external flow applications and the design of simplified propulsor models. For this purpose, a family of three grids, a coarse, a medium, and a fine mesh, were generated following the guidelines of the 6th AIAA Drag Prediction Workshop (DPW-6) [29]. Starting from the coarse mesh, the medium and fine mesh levels were obtained by consistently refining each curvilinear direction by factors of 1.4 and 2.0, respectively. The family of grids generated is depicted in Figure 17.

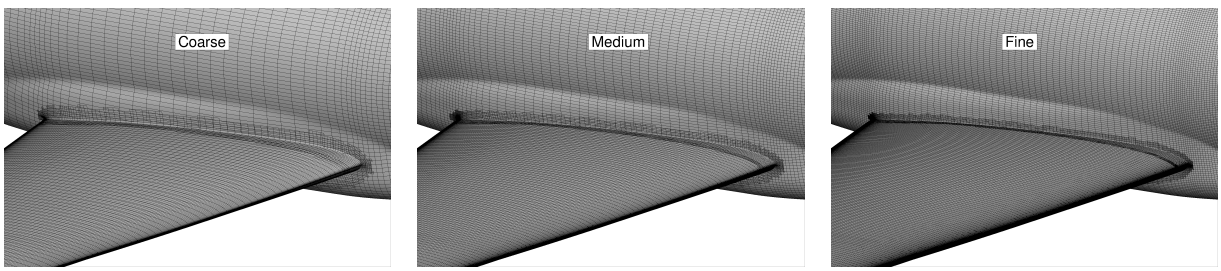

(a) Coarse mesh **(b) Medium mesh** **(c) Fine mesh**

Fig. 17 Grid refinement levels.

The grid convergence studies are presented in Figure 18 with the angle of attack and drag coefficient plotted against the square of the characteristic grid size $N^{-1/3}$, where N is the number of solution nodes. A linear relationship is expected given the second-order accurate spacial discretization utilized in this work. Here, it is possible to observe that both variables closely follow the expected second-order order convergence behavior, and that a reduction in solution sensitivity is observed with increased mesh refinement.

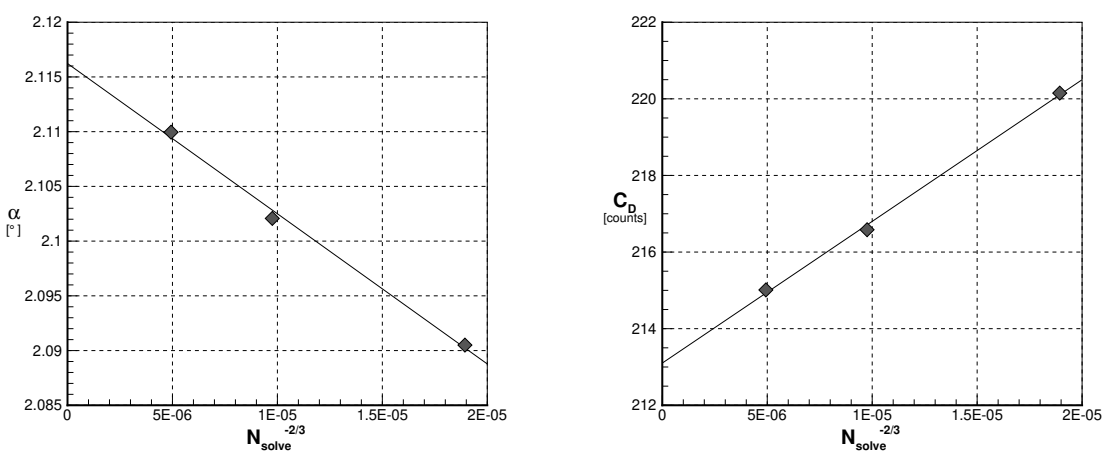

(a) Angle of attack **(b) Drag coefficient**

Fig. 18 Grid convergence plots.

A quantitative analysis of these results is presented in Table 5, where the extrapolated value of an infinitely fine mesh assuming a second-order order monotonic convergence is presented along with the grid characteristics. All three grid levels lay within 1.2% and 3.3% of the asymptotic value for angle of attack and drag coefficient, respectively. However, the computational resources required for these simulations using 10 Intel Broadwell nodes increase considerably in wall-time as the grids are refined.

Table 5 Grid refinement study results.

Grid Level	Solution Nodes [$\times 10^6$]	y^+_{avg}	Stretching Ratio[a]	α [°]	C_L	C_D [counts]	Walltime[b] [hr]
Coarse	12.13	0.78	1.20	2.091	0.50	220.2	0.09
Medium	32.81	0.56	1.14	2.102	0.50	216.6	0.39
Fine	91.24	0.39	1.09	2.110	0.50	215.0	1.12
∞	–	–	–	2.116	0.50	213.1	–

[a]Wall normal.

[b]Utilizing 10 Intel Broadwell nodes.

In order to corroborate the conclusions provided by the integrated loads, surface pressure distributions are also assessed at several spanwise locations along the wing. These results are presented in Figure 19, where an excellent agreement between all three mesh levels can be seen despite minor differences in the upper surface shock strengths and locations toward the outboard portion of the wing. Based on these observations, all three refinement levels are appropriate for further analysis given the similar predictions of the flow features and integrated loads, at least where external aerodynamics are concerned. However, the medium mesh resolution is selected for subsequent studies given its higher accuracy over the coarse mesh at a small cost increase of only 0.3 walltime hours.

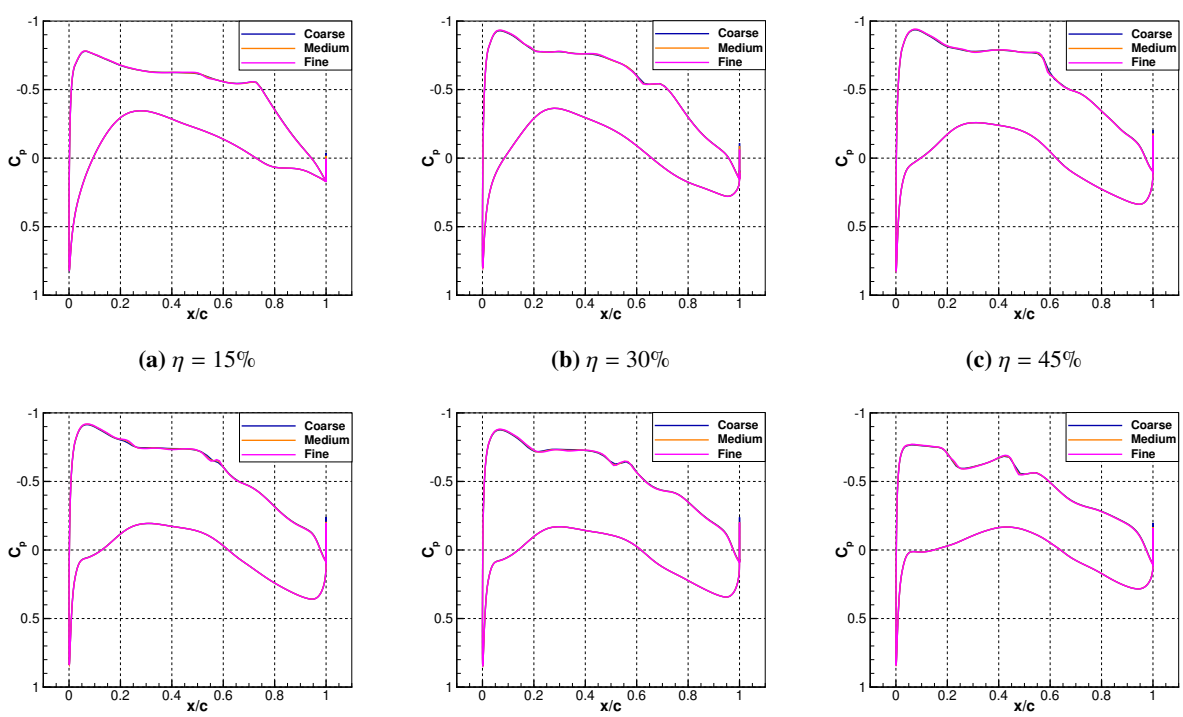

(a) η = 15% **(b)** η = 30% **(c)** η = 45%

(d) η = 60% **(e)** η = 75% **(f)** η = 90%

Fig. 19 Surface pressure distributions at various spanwise locations.